

# A Robust Immersed Boundary-Lattice Boltzmann Method for Simulation of Fluid-Structure Interaction Problems

Jie Wu\*, Jing Wu, Jiapu Zhan, Ning Zhao and Tongguang Wang

*Department of Aerodynamics, Nanjing University of Aeronautics and Astronautics,  
Yudao Street 29, Nanjing 210016, Jiangsu, China.*

Communicated by Kun Xu

Received 18 January 2015; Accepted (in revised version) 21 July 2015

---

**Abstract.** A robust immersed boundary-lattice Boltzmann method (IB-LBM) is proposed to simulate fluid-structure interaction (FSI) problems in this work. Compared with the conventional IB-LBM, the current method employs the fractional step technique to solve the lattice Boltzmann equation (LBE) with a forcing term. Consequently, the non-physical oscillation of body force calculation, which is frequently encountered in the traditional IB-LBM, is suppressed greatly. It is of importance for the simulation of FSI problems. In the meanwhile, the no-slip boundary condition is strictly satisfied by using the velocity correction scheme. Moreover, based on the relationship between the velocity correction and forcing term, the boundary force can be calculated accurately and easily. A few test cases are first performed to validate the current method. Subsequently, a series of FSI problems, including the vortex-induced vibration of a circular cylinder, an elastic filament flapping in the wake of a fixed cylinder and sedimentation of particles, are simulated. Based on the good agreement between the current results and those in the literature, it is demonstrated that the proposed IB-LBM has the capability to handle various FSI problems effectively.

**PACS:** 47.11.-j, 47.15.-x, 47.85.-g

**Key words:** Immersed boundary-lattice Boltzmann method, fractional step, suppression of force non-physical oscillation, fluid-structure interaction.

---

## 1 Introduction

Fluid-structure interaction (FSI) problems are constantly observed in both nature and engineering applications. Some examples are flapping motion of flags in the wind, deformation of red blood cells, transportation of solid particles, and so on. Many of these

---

\*Corresponding author. *Email addresses:* wuj@nuaa.edu.cn (Jie Wu), wujing\_04@126.com (Jing Wu), jiapuzhan@163.com (J. Zhan), zhaoam@nuaa.edu.cn (N. Zhao), tggwang@nuaa.edu.cn (T. Wang)

applications involve unsteady flows together with complex configurations, and their fundamental understanding is of critical importance. To numerically solve such problems, common approaches are to use either body-fitted meshes or fixed meshes. For the former approaches [1–3], the major difficulty is that a frequent mesh regeneration process is required that consequently increases the computational cost, particularly as complex and/or three-dimensional geometries are considered. In contrast, the latter approaches can avoid such difficulty due to the use of a regular fixed mesh for discretization of flow field. In these approaches, the effect of the embedded body on the surrounding fluid is taken into account in the form of an additional body force. Owing to such simplicity, they are very popular for FSI problems with arbitrary geometries. Thereinto, the immersed boundary method (IBM) is a famous example.

The IBM was originally developed by Peskin [4] for the purpose of simulating the blood flow in the human heart. Its basic idea is that the boundary of body can be represented by a set of Lagrangian points, and the body forces acting on the Lagrangian points that represent the effect of boundary can be distributed into the surrounding flow field. Subsequently, the whole flow field is discretized and solved on a regular Cartesian mesh. Therefore, a key issue of IBM is the treatment of body force. Hitherto, there are two implementations developed. One is the ‘discrete forcing scheme’ wherein the body force is either explicitly or implicitly applied to the discrete governing equations of flow field [5–7]. This scheme possesses the precise satisfaction of the boundary condition at the body surface by maintaining a sharp interface representation. However, its implementation for complex geometries may suffer some challenges because it needs to identify the mesh point where the body force is located. The other is the ‘continuous forcing scheme’ wherein a continuous forcing function, such as a discrete delta function, around the boundary is added to the governing equations [8–10]. This scheme can be directly implemented in any solver with relative ease, and the body interface might be diffused because of the introduction of interpolation.

From the methodological point of view, the IBM can be regarded as a technique for boundary treatment. Meanwhile, the flow field solution can be obtained by either solving the traditional Navier-Stokes (N-S) equations or using other approaches. One choice is the lattice Boltzmann method (LBM) that is an alternative to N-S solver with high simplicity and parallelism, and it has already been successfully applied to simulate various flow problems [11]. The coupling of IBM with LBM (i.e., IB-LBM) was first performed by Feng and Michaelides [12,13], and then it was used to simulate particulate flows. Thereafter, this method has been refined continually and utilized to handle a variety of FSI problems [14–23]. Currently, there are two ways to treat the body force in the IB-LBM, i.e., explicit and implicit. In the explicit treatment that has been popularly employed, the body force is calculated in advance by using the penalty method [12,15,16,19], direct forcing method [13] or momentum exchange method [14,22]. As a consequence, the no-slip boundary condition is only approximately satisfied, which may induce some flow penetration to body. In the implicit treatment, on the other hand, the body force is first set as unknown and then is obtained by solving a formed matrix directly [17,21] or ap-

plying the iteration procedure [18,20,23]. During this process, it is noted that the no-slip boundary has been incorporated.

For the FSI problems, the existing IB-LBM may suffer from the non-physical oscillation of body force calculation more or less. To overcome this deficiency, some attempt has been made. For example, Yang et al. [24] proposed a smoothened 4-point piecewise function to replace the traditional discrete delta function in IBM. Recently, Shu et al. [25] introduced the fractional step technique into the N-S equations. They found that the calculation of body force could converge to a steady state solution very fast. This feature is very attractive for the simulation of FSI problems because it can suppress the force oscillation and also can improve the stability and accuracy of numerical simulation. To the best of our knowledge, however, the fractional step technique has not yet been applied into the IB-LBM. In this study, a robust IB-LBM is presented in which the lattice Boltzmann equation (LBE) is solved with the help of the fractional step technique. Meanwhile, the body force is calculated implicitly. As a result, the present IB-LBM can not only satisfy the boundary condition strictly but also compute the body force with suppressed oscillation.

The paper is organized as follows. The robust IB-LBM is introduced in Section 2. It is followed by some validation tests. Section 4 presents the detailed simulations of different FSI problems, including the vortex-induced vibration of a circular cylinder, an elastic filament flapping in the wake of a fixed cylinder and sedimentation of particles. Finally, concluding remarks are presented in Section 5.

## 2 A robust immerse boundary-lattice Boltzmann method

For a two-dimensional viscous incompressible flow over an immersed object, the governing equations for the fluid flow in the IBM framework can be written as

$$\rho_f \left( \frac{\partial \mathbf{u}}{\partial t} + \mathbf{u} \cdot \nabla \mathbf{u} \right) + \nabla p = \mu \Delta \mathbf{u} + \mathbf{f}, \quad (2.1)$$

$$\nabla \cdot \mathbf{u} = 0, \quad (2.2)$$

where  $\rho_f$ ,  $\mathbf{u}$  and  $p$  are the fluid density, velocity and pressure, respectively.  $\mathbf{f}$  is the body force applied to satisfy the no-slip boundary condition on the immersed object. The formulation of  $\mathbf{f}$  will be provided later. When the fluid field is alternatively resolved by using LBM, the corresponding equation can be expressed as

$$f_\alpha(\mathbf{x} + \mathbf{e}_\alpha \delta t, t + \delta t) - f_\alpha(\mathbf{x}, t) = -\frac{1}{\tau} (f_\alpha(\mathbf{x}, t) - f_\alpha^{eq}(\mathbf{x}, t)) + F_\alpha \delta t, \quad (2.3)$$

$$F_\alpha = \left( 1 - \frac{1}{2\tau} \right) w_\alpha \left( \frac{\mathbf{e}_\alpha - \mathbf{u}}{c_s^2} + \frac{\mathbf{e}_\alpha \cdot \mathbf{u}}{c_s^4} \mathbf{e}_\alpha \right) \cdot \tilde{\mathbf{f}}, \quad (2.4)$$

where  $f_\alpha$  is the distribution function, and  $f_\alpha^{eq}$  is its corresponding equilibrium state;  $\tau$  is the single relaxation parameter;  $\delta t$  is the time step;  $\mathbf{e}_\alpha$  is the lattice velocity;  $w_\alpha$  and  $c_s$

respectively represent coefficients and sound speed that are related to the lattice velocity model used.  $\tilde{\mathbf{f}}$  is a force density related to the body force.

In the conventional IB-LBM, the body force is explicitly calculated [12–16, 19, 22]. The major limitation of these methods is that the velocity at the boundary point obtained from the flow field cannot be strictly equal to the boundary velocity required. It implies that the no-slip boundary condition is approximately satisfied. To overcome this problem, Shu et al. [25] proposed a velocity correction scheme to enforce the boundary condition. Later, this idea was applied by Wu et al. [17, 26–28] to simulate various stationary and moving boundary problems. Different from the work of Shu et al. [25], the body force could be directly computed from the velocity correction in the work of Wu et al. [17, 26–28]. However, the non-physical oscillation of body force computation is observed, which is similar to the conventional IB-LBM. As indicated by Shu et al. [25], to solve the governing equations (2.1) and (2.2) by using the fractional step technique, the computation of body force could converge to a steady state solution very fast. This feature is appealing for the FSI problems and it can improve the stability and accuracy of numerical simulation.

Inspired by the work of Shu et al. [25], the governing equation of IB-LBM is also solved by using the fractional step technique in this study. As a result, Eq. (2.3) can be rewritten as

$$\tilde{f}_\alpha(\mathbf{x} + \mathbf{e}_\alpha \delta t, t + \delta t) - f_\alpha(\mathbf{x}, t) = -\frac{1}{\tau} (f_\alpha(\mathbf{x}, t) - f_\alpha^{eq}(\mathbf{x}, t)), \quad (2.5a)$$

$$f_\alpha(\mathbf{x}, t + \delta t) = \tilde{f}_\alpha(\mathbf{x}, t) + F_\alpha \delta t, \quad (2.5b)$$

where  $\tilde{f}_\alpha$  is the intermediate distribution function. By first solving Eq. (2.5a), the intermediate velocity can be obtained. That is

$$\mathbf{u}^* = \frac{1}{\rho_f} \sum_\alpha \mathbf{e}_\alpha \tilde{f}_\alpha, \quad \rho_f = \sum_\alpha \tilde{f}_\alpha. \quad (2.6)$$

As shown in the work of Wu and Shu [17], the velocity at the boundary point interpolated from the intermediate velocity does not satisfy the boundary condition. Therefore, the velocity correction technique should be employed to enforce the boundary condition. Same as the work of Wu and Shu [17], an unknown fluid velocity correction vector  $\delta \mathbf{u}$  is first defined. It is determined from the boundary velocity correction vector  $\delta \mathbf{u}_B$ . Thus, the final system of equations about  $\delta \mathbf{u}_B$  can be written as,

$$\mathbf{A}\mathbf{X} = \mathbf{B}, \quad (2.7)$$

where

$$\begin{aligned} \mathbf{X} &= \left\{ \delta \mathbf{u}_B^1, \delta \mathbf{u}_B^2, \dots, \delta \mathbf{u}_B^m \right\}^T; \\ \mathbf{A} &= \begin{pmatrix} \delta_{11} & \delta_{12} & \cdots & \delta_{1n} \\ \delta_{21} & \delta_{22} & \cdots & \delta_{2n} \\ \vdots & \vdots & \ddots & \vdots \\ \delta_{m1} & \delta_{m2} & \cdots & \delta_{mn} \end{pmatrix} \begin{pmatrix} \delta_{11}^B & \delta_{12}^B & \cdots & \delta_{1m}^B \\ \delta_{21}^B & \delta_{22}^B & \cdots & \delta_{2m}^B \\ \vdots & \vdots & \ddots & \vdots \\ \delta_{n1}^B & \delta_{n2}^B & \cdots & \delta_{nm}^B \end{pmatrix}; \\ \mathbf{B} &= \begin{pmatrix} \mathbf{U}_B^1 \\ \mathbf{U}_B^2 \\ \vdots \\ \mathbf{U}_B^m \end{pmatrix} - \begin{pmatrix} \delta_{11} & \delta_{12} & \cdots & \delta_{1n} \\ \delta_{21} & \delta_{22} & \cdots & \delta_{2n} \\ \vdots & \vdots & \ddots & \vdots \\ \delta_{m1} & \delta_{m2} & \cdots & \delta_{mn} \end{pmatrix} \begin{pmatrix} \mathbf{u}_1^* \\ \mathbf{u}_2^* \\ \vdots \\ \mathbf{u}_n^* \end{pmatrix}. \end{aligned}$$

Here  $m$  is the number of the boundary points, and  $n$  is the number of the surrounding Eulerian mesh points.  $\delta \mathbf{u}_B^l$  ( $l = 1, 2, \dots, m$ ) is the unknown boundary velocity correction vector, and  $\delta_{ij} = D_{ij}(\mathbf{x}_{ij} - \mathbf{X}_B^l) \Delta x \Delta y$  together with  $\delta_{ij}^B = D_{ij}(\mathbf{x}_{ij} - \mathbf{X}_B^l) \Delta s_l$ .  $D_{ij}(\mathbf{x}_{ij} - \mathbf{X}_B^l)$  is the discrete delta function, which is used to connect the flow field to the boundary.  $\mathbf{x}_{ij}$  and  $\mathbf{X}_B^l$  are Eulerian coordinates and boundary points coordinates, respectively. In this study, a smoothened 4-point piecewise function proposed by Yang et al. [24] is chosen. It can be expressed as

$$D_{ij}(\mathbf{x}_{ij} - \mathbf{X}_B^l) = \frac{1}{h^2} \delta \left( \frac{x_{ij} - X_B^l}{h} \right) \delta \left( \frac{y_{ij} - Y_B^l}{h} \right), \quad (2.8)$$

$$\delta(r) = \begin{cases} \frac{3}{8} + \frac{\pi}{32} - \frac{r^2}{4}, & |r| \leq 0.5, \\ \frac{1}{4} + \frac{1-|r|}{8} \sqrt{-2+8|r|-4r^2} - \frac{1}{8} \arcsin \left( \sqrt{2}(|r|-1) \right), & 0.5 < |r| < 1.5, \\ \frac{17}{16} - \frac{\pi}{64} - \frac{3|r|}{4} + \frac{r^2}{8} + \frac{|r|-2}{16} \sqrt{-14+16|r|-4r^2} \\ \quad + \frac{1}{16} \arcsin \left( \sqrt{2}(|r|-2) \right), & 1.5 < |r| < 2.5, \\ 0, & |r| > 2.5. \end{cases} \quad (2.9)$$

In the above equations,  $h$  is the mesh spacing,  $\Delta s_l$  is the arc length of boundary element, and  $\mathbf{U}_B^l$  is the boundary velocity. By solving equation system (2.7), the boundary velocity correction vector  $\delta \mathbf{u}_B$  can be obtained, and the corresponding fluid velocity correction vector  $\delta \mathbf{u}$  can be further obtained by using the piecewise function (2.8). As a consequence, the corrected fluid velocity, i.e.,  $\mathbf{u} = \mathbf{u}^* + \delta \mathbf{u}$ , can strictly satisfy the boundary condition. In addition, it is noted the corrected fluid velocity is related to the force density [17], i.e.,  $\rho_f \mathbf{u} = \rho_f \mathbf{u}^* + \tilde{\mathbf{f}} \delta t / 2$ . Thus, the fluid velocity correction and force density has a following relationship

$$\tilde{\mathbf{f}} = 2\rho_f \delta \mathbf{u} / \delta t. \quad (2.10)$$

After obtaining the force density  $\tilde{\mathbf{f}}$ , the distribution function is updated by using Eq. (2.5b). Subsequently, other macroscopic variables can be calculated by using the following rela-

tionships,

$$\rho_f = \sum_{\alpha} f_{\alpha}, \quad P = c_s^2 \rho_f. \quad (2.11)$$

In fact, it is found the density calculated from the updated distribution in Eq. (2.11) is the same as that in Eq. (2.6). On the other hand, applying the Chapman-Enskog expansion [11] to Eqs. (2.5a) and (2.5b), the following equations can be obtained

$$\rho_f \left( \frac{\partial \mathbf{u}}{\partial t} + \mathbf{u} \cdot \nabla \mathbf{u} \right) = -\nabla p + \mu \Delta \mathbf{u}, \quad (2.12a)$$

$$\rho_f \frac{\partial \mathbf{u}}{\partial t} = \left( 1 - \frac{1}{2\tau} \right) \tilde{\mathbf{f}} = \mathbf{f}. \quad (2.12b)$$

It is noted that Eqs. (2.12a) and (2.12b) are the results by applying the fractional step technique to Eq. (2.1). Substituting Eq. (2.10) into Eq. (2.12b), the body force in the current method is calculated by

$$\mathbf{f} = \left( 1 - \frac{1}{2\tau} \right) \tilde{\mathbf{f}} = \left( 2 - \frac{1}{\tau} \right) \rho_f \delta \mathbf{u} / \delta t. \quad (2.13)$$

Similarly, the calculation of boundary force  $\mathbf{F}_B$  can be expressed as

$$\mathbf{F}_B = \left( 2 - \frac{1}{\tau} \right) \rho_f \delta \mathbf{u}_B / \delta t. \quad (2.14)$$

This determines the force exerted on the fluid that is balanced by the hydrodynamic force  $\mathbf{F}_f$  exerted on the boundary, i.e.,  $\mathbf{F}_f = -\sum_l \mathbf{F}_B^l \Delta s_l$ . Compared with the conventional IB-LBM, the current method can exactly satisfy the no-slip boundary condition. Moreover, it also can more stably calculate the force acting on the immersed boundary compared with the previous IB-LBM [17]. Thus, the present IB-LBM can be applied to accurately and efficiently deal with both stationary and moving boundary problems.

In summary, the numerical implementation of the present IB-LBM can be outlined below

- Step 1: Generate computational mesh and set initial values;
- Step 2: Compute the matrix  $\mathbf{A}$  and get its inverse matrix  $\mathbf{A}^{-1}$ ;
- Step 3: Use Eq. (2.5a) to obtain the distribution function and use Eq. (2.6) to compute the intermediate velocity;
- Step 4: Solve Eq. (2.7) to get the boundary velocity correction and subsequently compute the corrected fluid velocity;
- Step 5: Obtain the force density using Eq. (2.10) and solve Eq. (2.5b) to update the distribution function;
- Step 6: Solve Eq. (2.14) to obtain the boundary force and get the corresponding hydrodynamic force;
- Step 7: Repeat Step 2 to 6 until convergence is reached.

### 3 Numerical validation

Since the proposed IB-LBM can be used to deal with both stationary and moving boundary problems, the flows over a fixed circular cylinder and a transversely oscillating circular cylinder are simulated to perform the validation.

#### 3.1 Flow over a fixed circular cylinder

The flow over a fixed circular cylinder has been studied for a long time and now it is always used to validate the developed numerical method. Depending on the Reynolds number, which is generally defined by using the diameter of cylinder  $D$  and freestream velocity  $U_\infty$ , different flow patterns (i.e., steady flow and unsteady flow) can be observed. For the steady flow (i.e.,  $Re < 49$ ), a pair of steady separation bubbles behind the cylinder can be observed. For the unsteady flow, a well-known periodic Karman vortex street occurs. In the current simulation, four Reynolds numbers, namely  $Re=20, 40$  and  $100$  and  $200$  are selected. The computational domain size is  $50D \times 40D$ . A non-uniform mesh is used, in which the mesh for the region around the cylinder (the region size is  $1.2D \times 1.2D$ ) is uniform and its mesh spacing is denoted as  $h$ . The equilibrium distribution functions are used to implement the far field boundary conditions.

To measure the flow characteristics, three parameters can be used. They are drag and lift coefficients and Strouhal number, which are respectively defined as

$$C_d = 2F_f^D / (\rho_\infty U_\infty^2 D), \quad C_l = 2F_f^L / (\rho_\infty U_\infty^2 D), \quad (3.1a)$$

$$St = fD / U_\infty \quad (3.1b)$$

where  $F_f^D$  and  $F_f^L$  are the drag and lift forces acting on the cylinder respectively, which can be computed based on Eq. (2.14);  $f$  is the vortex shedding frequency for the unsteady flow;  $\rho_\infty$  is the freestream density.

Table 1 lists the time-averaged drag coefficient, lift coefficient and Strouhal number for all the Reynolds numbers considered. In addition, to perform the convergence validation, the current results with different values of uniform mesh spacing  $h$  are presented. From the results shown in this table, it is evident that the current results compare well with the data in the literature [22, 23, 29, 30]. Moreover, it is known accurate results can be obtained when the mesh spacing of uniform mesh is  $h = D/80$ .

Since the no-slip boundary condition is strictly satisfied in the present IB-LBM, the flow penetration to body should not occur. Fig. 1 shows the streamlines obtained by using the current method for the cases of  $Re = 20$  and  $40$  when the flows reach their steady states. It can be found from the figure that the streamlines are clearly separated by the cylinder surface. As a consequence, the streamlines outside the cylinder can safely pass through the cylinder without penetration, and the streamlines inside the cylinder are well enclosed.

To demonstrate the fast convergence feature of body force calculation of the present IB-LBM, Fig. 2 plots the time evolution of the drag coefficient at  $Re = 20$ , where the time

Table 1: Comparison of the time-average drag coefficient  $\bar{C}_d$ , lift coefficient  $C_l$  and Strouhal number  $St$  for the flow over a fixed circular cylinder.

Refs.		$Re$							
		20	40	100			200		
		$\bar{C}_d$	$\bar{C}_d$	$\bar{C}_d$	$C_l$	$St$	$\bar{C}_d$	$C_l$	$St$
Yuan et al. [22]		2.07	1.56	1.40	0.34	0.160	1.40	0.67	0.190
Hu et al. [23]		2.21	1.66	1.42	0.37	0.166	1.39	0.71	0.195
Xu and Wang [29]		2.23	1.66	1.42	0.34	0.171	1.42	0.66	0.202
Gao et al. [30]		2.09	1.58	1.39	-	0.169	1.39	-	0.204
Present	$h = D/60$	2.12	1.63	1.42	0.28	0.171	1.46	0.67	0.201
	$h = D/80$	2.08	1.58	1.39	0.32	0.167	1.42	0.63	0.198
	$h = D/100$	2.07	1.56	1.37	0.31	0.166	1.42	0.62	0.196

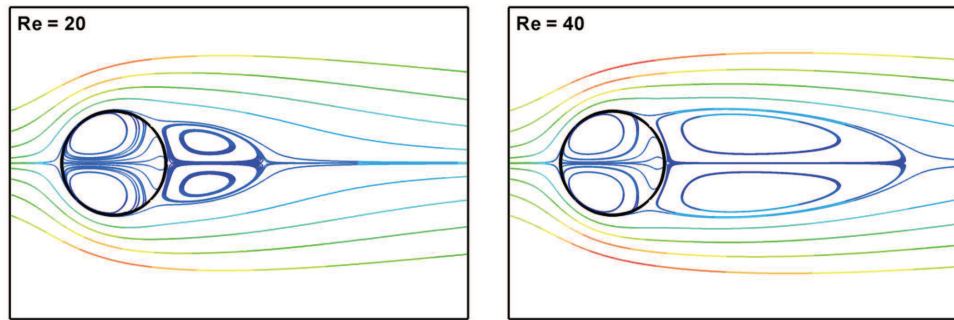


Figure 1: Streamlines of present IB-LBM for the flow over a fixed circular cylinder at  $Re=20$  and 40.

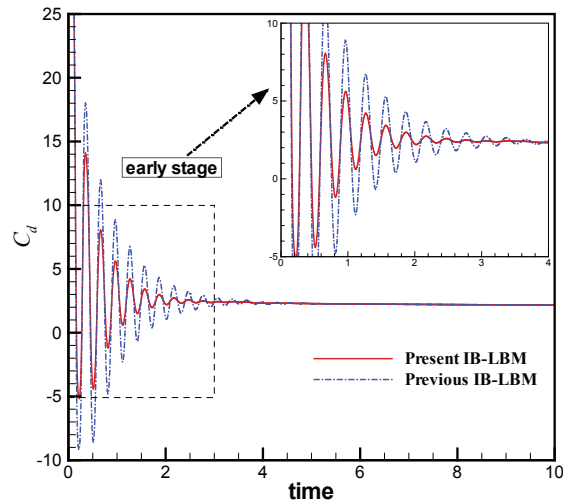


Figure 2: Comparison of time evolution of drag coefficient for the flow over a fixed circular cylinder at  $Re=20$ . The previous IB-LBM in Ref. [17] is used.



is nondimensionalized by  $D$  and  $U_\infty$ . From the results shown in this figure, it is clear that the current method can converge faster to the steady solution than the previous IB-LBM in [17] thanks to the fractional step technique, which is helpful for the suppression of force oscillation.

### 3.2 Flow over a transversely oscillating circular cylinder

To further validate the proposed IB-LBM, the flow over a transversely oscillating circular cylinder is simulated. This problem has been investigated experimentally and numerically and some interesting phenomena have been reported. For example, the vortex shedding frequency can synchronize with the oscillation frequency, which is now known as the lock-in of the vortex shedding. In the current simulation, the Reynolds number is fixed at  $Re = 185$ . The motion of the cylinder is imposed as  $y(t) = A \sin(2\pi f_e t)$ , with  $y(t)$  the transverse displacement of the cylinder,  $A$  the amplitude of the oscillation, and  $f_e$  the oscillation frequency. For comparison, the parameters used in this study are the same as those of Yang and Stern [31], i.e.,  $A = 0.2D$  and  $f_e/f_0 = 0.8, 1.0, 1.1, 1.2$ , with  $f_0$  the natural vortex shedding frequency for a fixed circular cylinder (The corresponding Strouhal number based on the current method is  $St_0 = 0.195$ ). The computational domain size is  $50D \times 40D$ . A non-uniform mesh is used, in which the mesh for the region around the cylinder (the region size is  $1.2D \times 1.6D$ ) is uniform with the mesh spacing of  $h = D/80$ .

Fig. 3 illustrates the instantaneous vorticity contours as the cylinder reaches the mid-point position in the process of downstroke. With the increase of  $f_e$ , the distance of shed vortices along the streamwise direction decreases gradually, and the strength of vortices

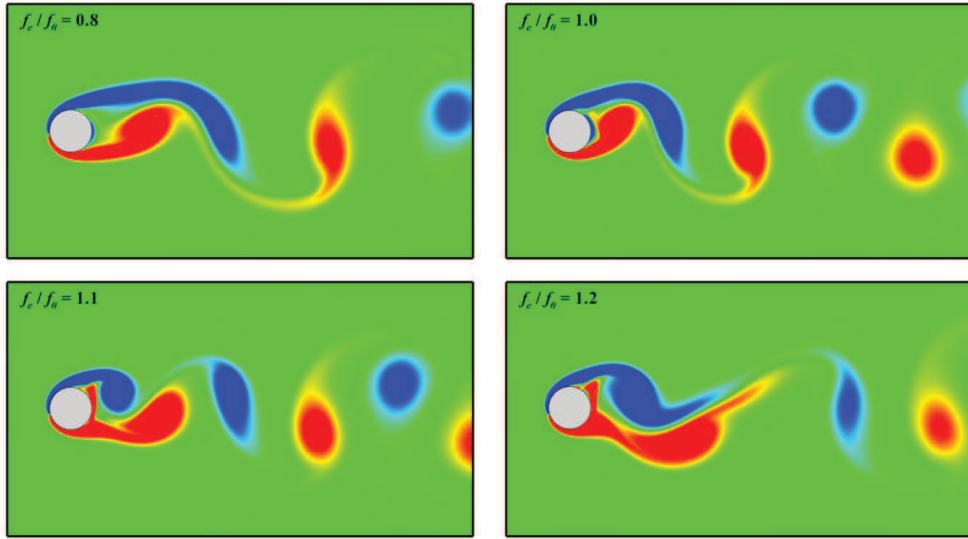


Figure 3: Instantaneous vorticity contours for the flow over a transversely oscillating circular cylinder at  $Re=185$  with different oscillation frequencies.

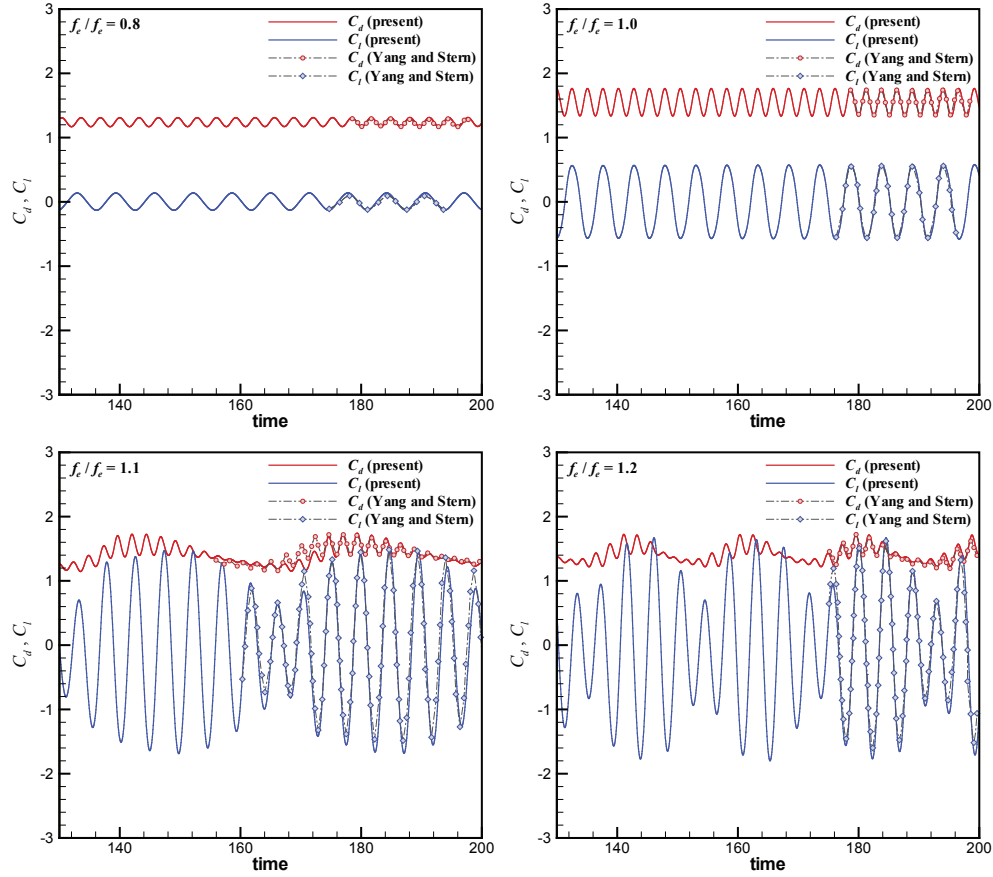


Figure 4: Time evolution of drag and lift coefficients for the flow over a transversely oscillating circular cylinder at  $Re = 185$  with different oscillation frequencies. The results of Yang and Stern [31] are included.

in the near wake is enhanced. Similar flow patterns can be found in the work of Yang and Stern [31].

Fig. 4 shows the time evolution of drag and lift coefficients with different oscillation frequencies. To make comparison, the results of Yang and Stern [31] are included. At  $f_e/f_0 = 0.8$  and  $1.0$ , the single harmonic variation of  $C_d$  and  $C_l$  can be observed, which is similar to the fixed cylinder case. At  $f_e/f_0 = 1.1$  and  $1.2$ , however,  $C_d$  and  $C_l$  vary periodically with multiple harmonics. In general, the current results have good agreement with those in [31].

To further display the effective suppression of body force, Fig. 5 compares the phase diagram of the drag coefficient and transverse cylinder displacement calculated by the present IB-LBM and previous IB-LBM [17] at  $f_e/f_0 = 0.8$ . Meanwhile, the results of Yang et al. [24] and Schneiders et al. [32] are also included. From the figure, it can be seen that the previous IB-LBM may produce the clear force oscillation and such oscillation can be

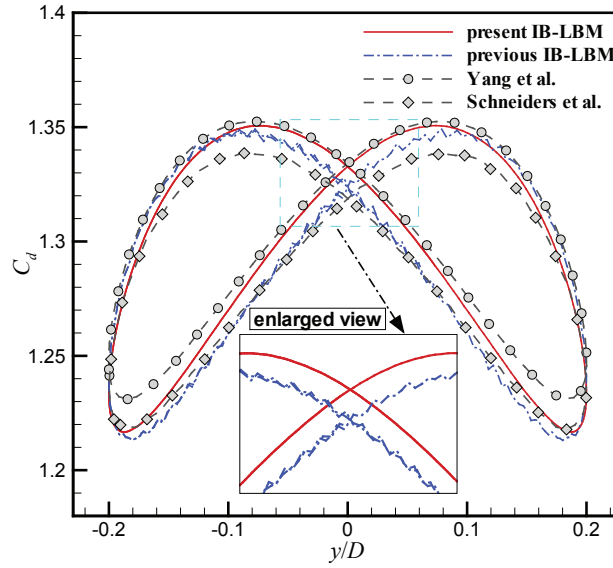


Figure 5: Phase diagram of the drag coefficient and transverse cylinder displacement at  $f_e/f_0 = 0.8$ . The previous IB-LBM in Ref. [17] is used.

greatly suppressed by the present IB-LBM. Thus, the current result compares well with the data from other numerical studies [24, 32].

Based on the obtained results in this section, it is inferred that the present IB-LBM is suitable for the simulation of both stationary and moving boundary problems. It can not only accurately satisfy the no-slip boundary condition but also effectively suppress the oscillation of body force calculation.

## 4 Simulations of FSI problems

After numerical validations with fixed boundary and imposed-motion moving boundary problems, the present IB-LBM is applied to handle different FSI problems. In this work, the vortex-induced-vibration of a circular cylinder, an elastic filament flapping in the wake of a fixed cylinder and sedimentation of particles are simulated.

### 4.1 Vortex-induced-vibration of a circular cylinder

When the fluid passes through a cylindrical structure, the resultant oscillatory forces may induce the structure to vibrate if it is elastically mounted. This behavior is well known as the vortex-induced vibration (VIV). Engineering problems associated with the VIV of cylindrical structures have been investigated in a wide range. Under some specific conditions, these structures are possibly damaged or even broken down.

For an elastically mounted circular cylinder with one degree of freedom (1-DOF) along the vertical direction, its motion is governed by the following equation

$$m_c \frac{d^2 y}{dt^2} + b \frac{dy}{dt} + ky = F_f^L, \quad (4.1)$$

where  $y$  is the vertical displacement of the cylinder;  $m_c$  is the mass of the cylinder;  $b$  is the damping coefficient;  $k$  is the spring stiffness. For the purpose of stimulating oscillation, the damping coefficient is set as  $b=0$  in this simulation. After the nondimensionalization, Eq. (4.1) can be rewritten as

$$\ddot{Y} + \left( \frac{2\pi}{U^*} \right)^2 Y = \frac{C_l}{2m^*}, \quad (4.2)$$

where  $Y=y/D$ ;  $U^*=U_\infty/f_n D$  is the reduced velocity of the cylinder which determines the response of the cylinder to fluid flow, where  $f_n=(1/2\pi)\sqrt{k/m_c}$  is the natural frequency of the cylinder;  $m^*=m_c/\rho_f D^2$  is the mass ratio of the cylinder to the fluid. To make comparison, the mass ratio is chosen as  $m^*=2$ , the reduced velocity  $U^*$  varies from 3 to 8, and the Reynolds number is  $Re=150$ . Such sets of parameters were also used in the previous work [33–35]. The computational domain size is  $50D \times 40D$ . A non-uniform mesh is used, in which the mesh for the region around the cylinder (the region size is  $1.2D \times 2.2D$ ) is uniform with the mesh spacing of  $h=D/80$ .

Fig. 6 the shows the variation of maximum displacement  $Y_{\max}$  as a function of the reduced velocity  $U^*$ . From this figure, it is seen that a sudden increase of  $Y_{\max}$  occurs at  $U^*=4$ , and then it starts to decrease gradually as  $U^*$  keeps increasing. Thereafter, a sharp drop of  $Y_{\max}$  is found at  $U^*=8$ . This variation trend, which shows good agreement with the results in the literature [33–35], is determined by the natural frequency of the

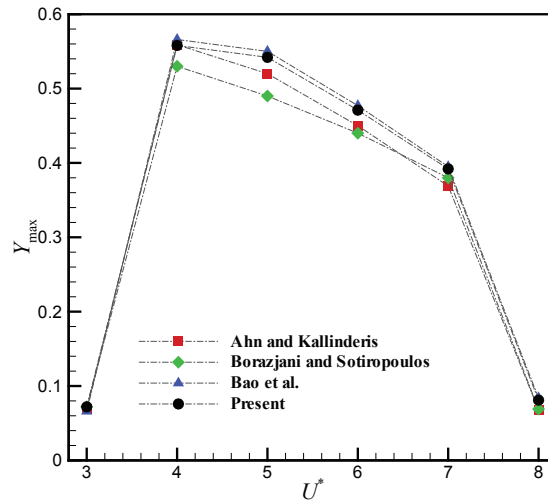


Figure 6: Comparison of the maximum displacement  $Y_{\max}$  for the VIV of a circular cylinder at  $Re=150$ .

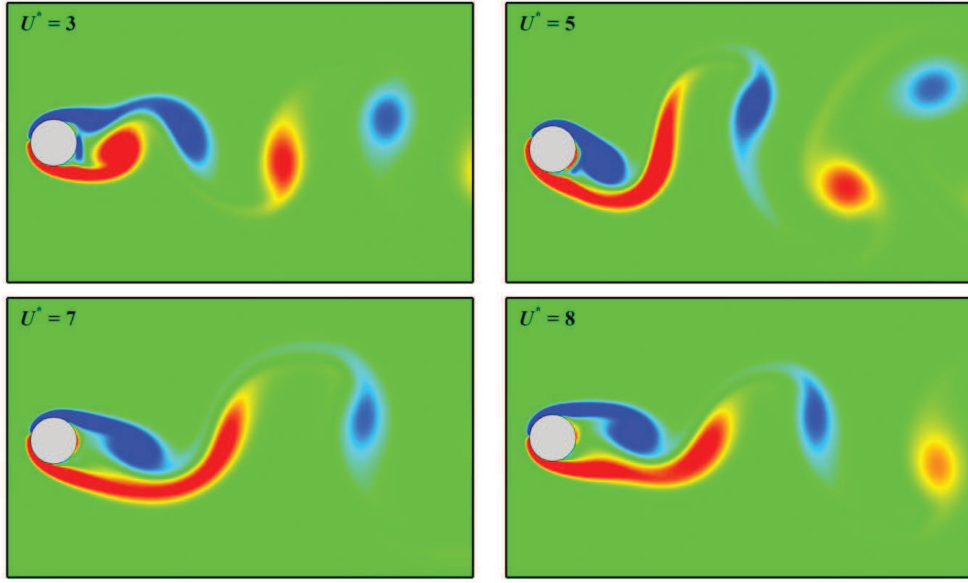


Figure 7: Instantaneous vorticity contours for the VIV of a circular cylinder at  $Re = 150$  with different reduced velocities.

cylinder. It has been proven that a large amplitude vibration (i.e.,  $Y_{\max} > 0.1$ ) occurs if the cylinder natural frequency (or  $U^*$ ) falls within the so-called lock-in region. Within this region ( $4 \leq U^* \leq 7$  of this case), the vortex shedding frequency always synchronizes with the cylinder oscillation frequency. Otherwise, the vibration amplitude is small (i.e.,  $Y_{\max} < 0.1$ ).

Fig. 7 shows some typical instantaneous vorticity contours as the cylinder reaches the midpoint position in the process of upstroke. At  $U^* = 3$  and 8 that correspond to the small vibration amplitude, a single-row vortex wake behind the cylinder is exhibited. At  $U^* = 5$ , which is within the lock-in region, a double-row vortex wake is formed. At  $U^* = 7$ , however, the wake configuration returns to the single-row vortex structure although the vibration amplitude is still large. Therefore, it is indicated that the change of wake configuration is independent to the transition of lock-in region. Similar flow patterns were also presented in the work of Bao et al. [35].

## 4.2 An elastic filament flapping in the wake of a fixed cylinder

In biofluid dynamics, a large number of problems include deformable elastic bodies. One example is the fish swimming. It is documented that the fish swimming in the wake of a fixed bluff body is able to extract the kinetic energy from the vortices generated by the body [36]. Such problem can roughly be simplified as the interaction between an elastic filament and a fixed cylinder, which has been numerically investigated in recent years [19, 22].

For a massive and inextensible filament with the length of  $L$ , its motion equation in the Lagrangian form can be written as [19,37]

$$\rho_s \frac{\partial^2 \mathbf{X}}{\partial t^2} - \frac{\partial}{\partial s} \left( T \frac{\partial \mathbf{X}}{\partial s} \right) + \frac{\partial^2}{\partial s^2} \left( K_b \frac{\partial^2 \mathbf{X}}{\partial s^2} \right) = \mathbf{F}_f, \quad (4.3)$$

where  $\mathbf{X}$  is the position vector of the filament,  $s$  is the Lagrangian coordinate along the filament length,  $\rho_s$  is the linear density of the filament,  $T$  is the tension force along the filament,  $K_b$  is the bending coefficient. At the fixed end of the filament, a simply supported condition can be used,

$$\frac{\partial^2 \mathbf{X}}{\partial s^2} = \mathbf{0}. \quad (4.4a)$$

At the free end of the filament, the condition reads

$$T = 0, \quad \frac{\partial^2 \mathbf{X}}{\partial s^2} = \mathbf{0}, \quad \frac{\partial^3 \mathbf{X}}{\partial s^3} = \mathbf{0}. \quad (4.4b)$$

To discretize Eq. (4.3), the scheme proposed by Huang et al. [37] is used in this study. It is briefly described as follows. First, the filament is initially discretized by  $m$  nodal points with equal arc length  $\Delta s = L/m$ . For  $l$ th nodal point ( $l = 0, 1, 2, \dots, m$ ), the temporal term is discretized as

$$\frac{\partial^2 \mathbf{X}}{\partial t^2} = \frac{\mathbf{X}_l^{N+1} - 2\mathbf{X}_l^N + \mathbf{X}_l^{N-1}}{\delta t^2}, \quad (4.5a)$$

where  $N$  means the time level. For the tension force term, it is discretized as

$$\frac{\partial}{\partial s} \left( T \frac{\partial \mathbf{X}}{\partial s} \right) = \frac{T_{l+\frac{1}{2}} \left( \frac{\mathbf{X}_{l+1}^{N+1} - \mathbf{X}_l^{N+1}}{\Delta s} \right) - T_{l-\frac{1}{2}} \left( \frac{\mathbf{X}_l^{N+1} - \mathbf{X}_{l-1}^{N+1}}{\Delta s} \right)}{\Delta s}, \quad (4.5b)$$

where the tension force  $T$  is determined by the constraint of inextensibility, i.e.,  $\partial \mathbf{X} / \partial s \cdot \partial \mathbf{X} / \partial s = 1$ . For the detail on how to calculate  $T$ , the reader can refer to the work of Huang et al. [37]. For the bending force term, it is discretized as

$$\frac{\partial^2}{\partial s^2} \left( K_b \frac{\partial^2 \mathbf{X}}{\partial s^2} \right) = K_b \frac{\mathbf{X}_{l+2}^* - 4\mathbf{X}_{l+1}^* + 6\mathbf{X}_l^* - 4\mathbf{X}_{l-1}^* + \mathbf{X}_{l-2}^*}{\Delta s^4}, \quad (4.5c)$$

where  $\mathbf{X}^* = 2\mathbf{X}^N - \mathbf{X}^{N-1}$  is used to reduce the error. After the position of the filament is updated, the velocity of the filament is computed by  $\mathbf{U}_B = (\mathbf{X}^{N+1} - \mathbf{X}^N) / \delta t$ .

In the current simulation, the length of the filament is set as  $L/D = 1$  and  $2.5$ ; the mass ratio of the filament to the fluid, defined as  $M = \rho_s / (\rho_f L)$ , is chosen as  $0.1$  and  $0.2$ ; the rigidity of the filament, defined as  $E_b = K_b / (\rho_f U_\infty^2 L^3)$ , is set to be on order of  $10^{-3}$ . The leading end of the filament is fixed and the trailing end is free to flap. The gap between the center of the cylinder and the leading end of the filament  $G$  is  $3D$ . The Reynolds

Table 2: Comparison of the time-average drag coefficient  $\bar{C}_d$  of the cylinder, the drag ratio  $\bar{C}_{d,f}/\bar{C}_{d,f_0}$  and the amplitude  $A/D$  and Strouhal number  $St_f$  of the filament.

Refs.	$(L/D, M)$	$\bar{C}_d$	$\bar{C}_{d,f}/\bar{C}_{d,f_0}$	$A/D$	$St_f$
Tian et al. [19]	Single cylinder	1.44	-	-	0.166
	(1, 0.1)	1.42	0.47	0.73	0.161
	(1, 0.2)	1.42	0.58	0.77	0.153
	(2.5, 0.1)	1.40	0.73	1.14	0.155
	(2.5, 0.2)	1.39	0.87	1.18	0.153
Yuan et al. [22]	Single cylinder	1.50	-	-	0.173
	(1, 0.1)	1.49	0.49	0.72	0.166
	(1, 0.2)	1.49	0.57	0.74	0.166
	(2.5, 0.1)	1.47	0.80	1.17	0.160
	(2.5, 0.2)	1.46	0.92	1.18	0.159
Present	Single cylinder	1.39	-	-	0.167
	(1, 0.1)	1.39	0.46	0.71	0.160
	(1, 0.2)	1.39	0.56	0.74	0.159
	(2.5, 0.1)	1.36	0.71	1.11	0.152
	(2.5, 0.2)	1.34	0.84	1.16	0.149

number based on the cylinder diameter is  $Re = 100$ . It is noted that the parameters used here are the same as those in other studied [19, 22]. The computational domain size is  $60D \times 40D$ . A non-uniform mesh is used, in which the meshes for the regions around the cylinder (the region size is  $1.2D \times 3D$ ) and filament (the region size is  $(L + 0.2D) \times 3D$ ) are uniform with the same mesh spacing of  $h = D/100$ .

Table 2 provides the mean coefficient  $\bar{C}_d$  of the cylinder, the drag ratio  $\bar{C}_{d,f}/\bar{C}_{d,f_0}$  and the amplitude of the filament  $A/D$  and the Strouhal number of the filament  $St_f$ . Here  $\bar{C}_{d,f}$  and  $\bar{C}_{d,f_0}$  respectively are the mean drag coefficient of the filament in the wake of the cylinder and mean drag coefficient of the corresponding filament in the absence of the cylinder. Since the filament flapping motion is induced by the cylinder vortices, the flapping frequency is the same as the vortex shedding frequency. It is known from the table that the introduction of a filament can slightly reduce the drag on the cylinder. Meanwhile, a clear reduction of vortex shedding frequency can be observed. On the other hand, the drag ratio  $\bar{C}_{d,f}/\bar{C}_{d,f_0}$  is always less than 1 for all the parameters considered. It implies that the filament achieves a drag reduction by staying in the cylinder wake. For a given length, the lighter filament can enjoy the more drag reduction, but the flapping amplitude is less sensitive to the filament mass. As the filament length increases, however, both the drag ratio and flapping amplitude increase. In general, the current results agree well with the data in the literature [19, 22].

Fig. 8 plots the typical profiles of the flapping filament in the cylinder wake and trajectory of the free end of the filament. The periodic variation of the filament can be found

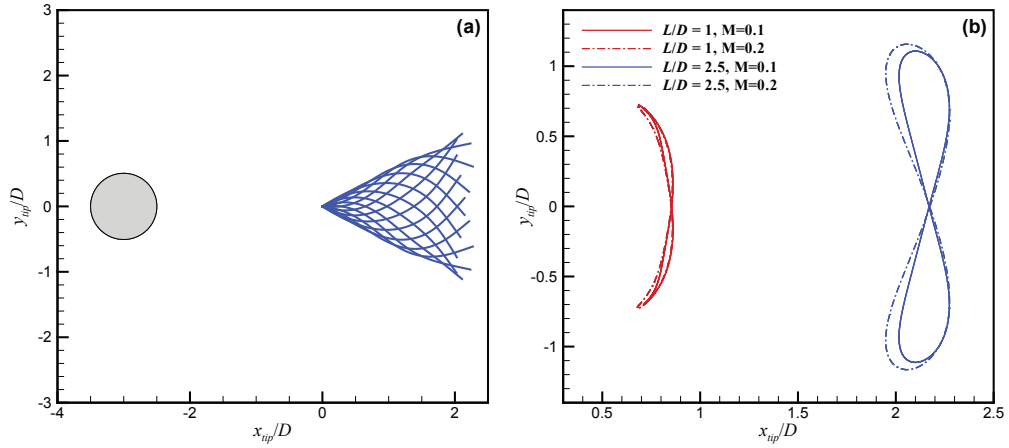


Figure 8: (a) Profiles of the flapping filament in the cylinder wake; (b) Trajectory of the free end of the filament for  $M=0.1$  and  $0.2$  at  $L/D=1$  and  $2.5$ .

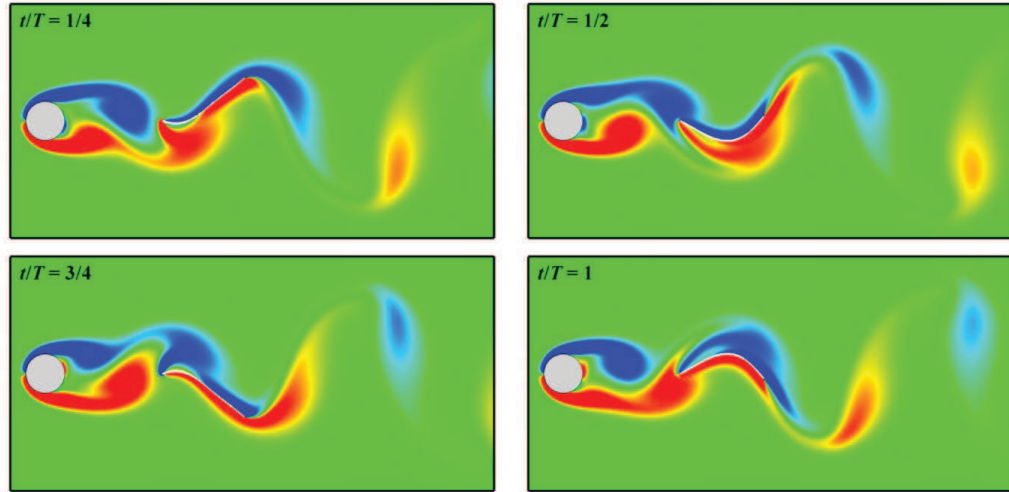


Figure 9: Evolution of the vorticity contours in one flapping period for  $M=0.2$  at  $L/D=2.5$ .

in the figure. At  $L/D = 1$ , the trajectory of free end of the filament forms an arc. At  $L/D = 2.5$ , the free end the filament draws an “eight” path. This phenomenon has also been found in [19,22].

Fig. 9 shows the time evolution of vorticity contours in one flapping period of the filament for  $M=0.1$  at  $L/D=2.5$ . At the instant of  $t=T/4$ , the free end of the filament reaches the highest position. One vortex shed from the cylinder has interacted with the fixed end of the filament and is moving downstream along the filament. After  $T/4$  interval, the filament tail comes to the midpoint position. Another cylinder vortex is interacting with the filament head. In the second half period, a similar change of vortices can be observed.



### 4.3 Sedimentation of particles

The particle-fluid interaction problems have been widely encountered in nature and engineering such as suspension and transport of sediment in river, cell transport in arteries and veins and fluidized bed reactors and so on.

In this work, the geometry of a particle is modeled as a circular cylinder. Considering a two-dimensional domain including  $N$  particles with the same size, the motion of  $i$ th particle is governed by

$$M_i \frac{d\mathbf{U}_R}{dt} = \mathbf{F}_i, \quad (4.6a)$$

$$I_i \frac{d\boldsymbol{\Omega}}{dt} = \mathbf{T}_i, \quad (4.6b)$$

where  $\mathbf{F}_i$  and  $\mathbf{T}_i$  are the total force and torque acting on the particle;  $\mathbf{U}_R$  and  $\boldsymbol{\Omega}$  are the translational and angular velocities of the particle, respectively;  $I_i$  is the moment inertia of the particle. The total force  $\mathbf{F}_i$  includes the gravity/buoyancy force, hydrodynamic force and particle collision force  $\mathbf{F}_i^{\text{col}}$ . Mathematically, it can be written as

$$\mathbf{F}_i = \left(1 - \frac{\rho_f}{\rho_p}\right) M_i \mathbf{g} + \mathbf{F}_f + \mathbf{F}_i^{\text{col}}, \quad (4.7a)$$

where  $M_i$  is the mass of the particle and  $\rho_p$  is the density of particle. The torque  $\mathbf{T}_i$  can be expressed as

$$\mathbf{T}_i = - \sum_l \left( \mathbf{X}_B^l - \mathbf{X}_R \right) \times \mathbf{F}_B^l \Delta s_l, \quad (4.7b)$$

where  $\mathbf{X}_R$  is the center of mass of the particle. Moreover, the particle collision force  $\mathbf{F}_i^{\text{col}}$  is implemented by using an artificial mechanism [14]

$$\mathbf{F}_i^{p-p} = \begin{cases} 0, & X_R^{i,j} > r_i + r_j + \zeta, \\ 2.4\epsilon \sum_{j=1, j \neq i}^N \left[ 2 \left( \frac{r_i + r_j}{X_R^{i,j}} \right)^{14} - \left( \frac{r_i + r_j}{X_R^{i,j}} \right)^8 \right] \frac{\mathbf{X}_R^i - \mathbf{X}_R^j}{(r_i + r_j)^2}, & X_R^{i,j} \leq r_i + r_j + \zeta, \end{cases} \quad (4.8a)$$

$$\mathbf{F}_i^{p-w} = \begin{cases} 0, & X_R^{i,w} > 2r_i + \zeta, \\ 2.4\epsilon \sum_{j=1}^N \left[ 2 \left( \frac{r_i}{X_R^{i,w}} \right)^{14} - \left( \frac{r_i}{X_R^{i,w}} \right)^8 \right] \frac{\mathbf{X}_R^i - \mathbf{X}_w}{(r_i)^2}, & X_R^{i,w} \leq 2r_i + \zeta, \end{cases} \quad (4.8b)$$

where  $\mathbf{F}_i^{p-p}$  and  $\mathbf{F}_i^{p-w}$  respectively denote the particle-particle and particle-wall collision forces,  $\epsilon = \left( \frac{2r_i r_j}{r_i + r_j} \right)^2$ ,  $r_i$  is radius of the particle,  $X_R^{i,j} = |\mathbf{X}_R^i - \mathbf{X}_R^j|$ ,  $X_R^{i,w} = |\mathbf{X}_R^i - \mathbf{X}_w|$ ,  $\mathbf{X}_w$  represents the wall position and  $\zeta$  is the threshold and is set to one lattice unit. Therefore, the final particle collision force is  $\mathbf{F}_i^{\text{col}} = \mathbf{F}_i^{p-p} + \mathbf{F}_i^{p-w}$ .

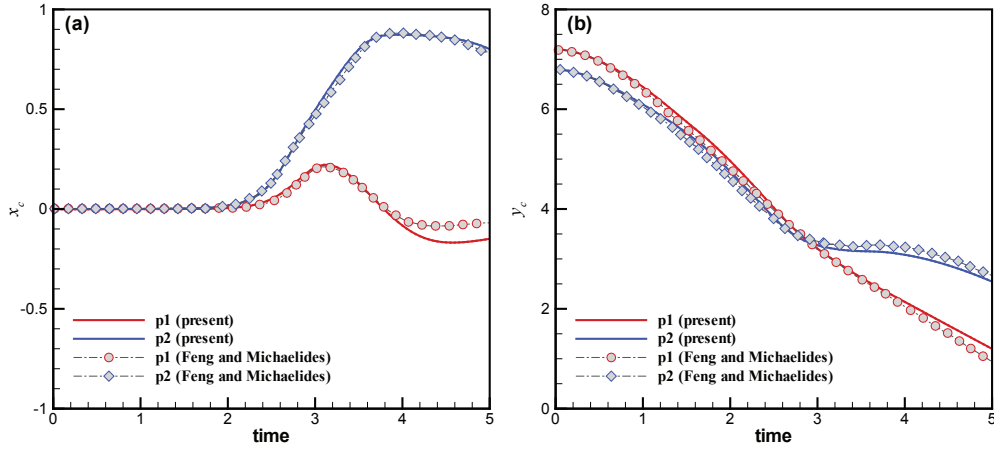
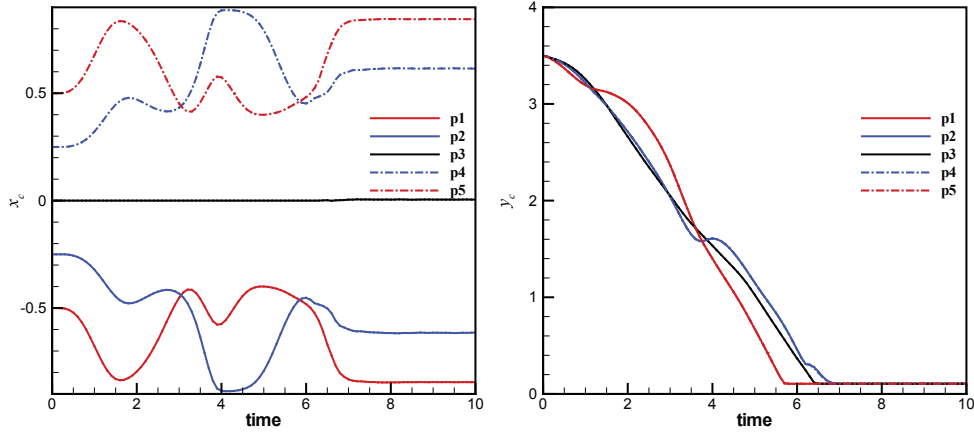


Figure 10: Evolution of the (a) horizontal position and (b) vertical position of particle center for sedimentation of two particles.

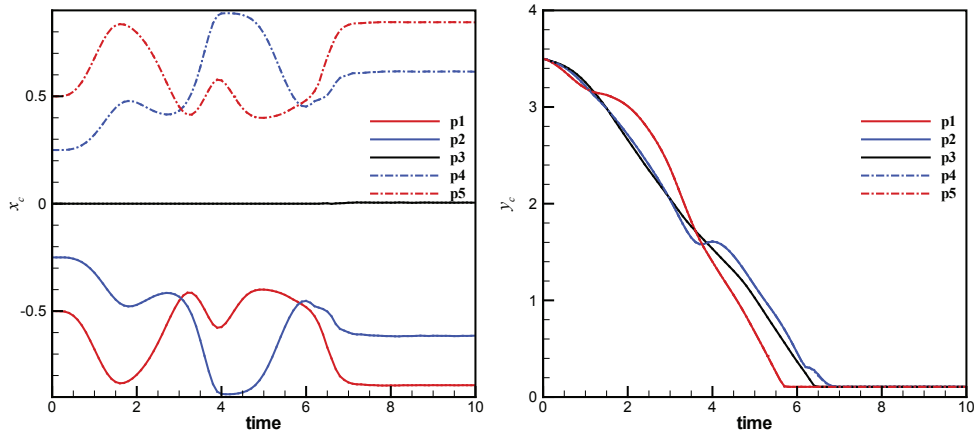
First, the sedimentation of two particles is simulated. A channel of width  $2\text{ cm}$  and height  $8\text{ cm}$  is considered. The properties of fluid are  $\mu = 0.001\text{ g/(cm}\cdot\text{s)}$  and  $\rho_f = 1.0\text{ (g/cm}^3\text{)}$ . Two particles possess the same properties. The density is  $\rho_p = 1.01\text{ (g/cm}^3\text{)}$  and the radius is  $r = 0.1\text{ cm}$ . Using the particle radius and density ratio of particle to fluid  $\rho_r (= \rho_p/\rho_f)$ , the reference velocity can be defined as  $U_{ref} = \sqrt{\pi r(\rho_r - 1)g}$  [38]. Initially, both fluid and particles are at rest. The first particle (p1) is set at  $(-0.001\text{ cm}, 7.2\text{ cm})$  and the other (p2) at  $(0\text{ cm}, 6.8\text{ cm})$ . It is noted the parameters used here are the same as those in the work of Feng and Michaelides [12]. The two particles start dropping under the gravity force. In this simulation, a uniform mesh is used with mesh size of  $201 \times 801$ . The bounce back scheme is used to implement the channel wall boundary conditions.

It is known that the two particles settled close to each other would go through drafting, kissing and tumbling or DKT motion [39]. Fig. 10 depicts the time evolution of the horizontal and vertical positions of two particle centers, together with the results of Feng and Michaelides [12], where the time is nondimensionalized by  $\mu, \rho_f$  and channel width. It can be found that these results are in good agreement until kissing and tumbling begin. As pointed out by Fortes et al. [39], the tumbling is essentially a breakup of an unstable configuration of the particle positions. Thus an exact agreement after kissing may not be expected.

Then, the sedimentation of five particles in a tank of width  $2\text{ cm}$  and height  $4\text{ cm}$  is simulated. The properties of fluid and particles are the same as those of two particles case above. Two initial sets of particles are considered and all the particles are placed in a line of height  $3.5\text{ cm}$ . For the first set, denoted as compact set, the horizontal positions of five particle centers are  $-0.5\text{ cm}, -0.25\text{ cm}, 0\text{ cm}, 0.25\text{ cm}$  and  $0.5\text{ cm}$ , respectively. For the second set, denoted as sparse set, the corresponding horizontal positions are  $-0.8\text{ cm}, -0.4\text{ cm}, 0\text{ cm}, 0.4\text{ cm}$  and  $0.8\text{ cm}$ , respectively.



(a) Compact set



(a) Sparse set

Figure 11: Evolution of the horizontal and vertical positions of particle center for sedimentation of five particles.

Fig. 11 presents the time evolution of the horizontal and vertical positions of particle centers. For both sets, the horizontal position of the third particle is nearly a constant that equals to  $0\text{cm}$ . Meanwhile, the motion of the second and fourth particles as well as the first and fifth particles is symmetric to the vertical centerline. For the compact set, the initial particle-particle repulsive force along the horizontal direction is large. As the sedimentation begins, such force pushes the first and second particles to the left wall at the early stage. Due to the large particle-wall repulsive force, the first particle then moves towards the vertical centerline, and even pushes the second particle to the left wall, which means that the first and second particles switch their positions. Before they reach the bottom of the tank, they switch their positions again due to the large particle-wall repulsive force. A similar variation process occurs synchronously for the fourth and fifth particles

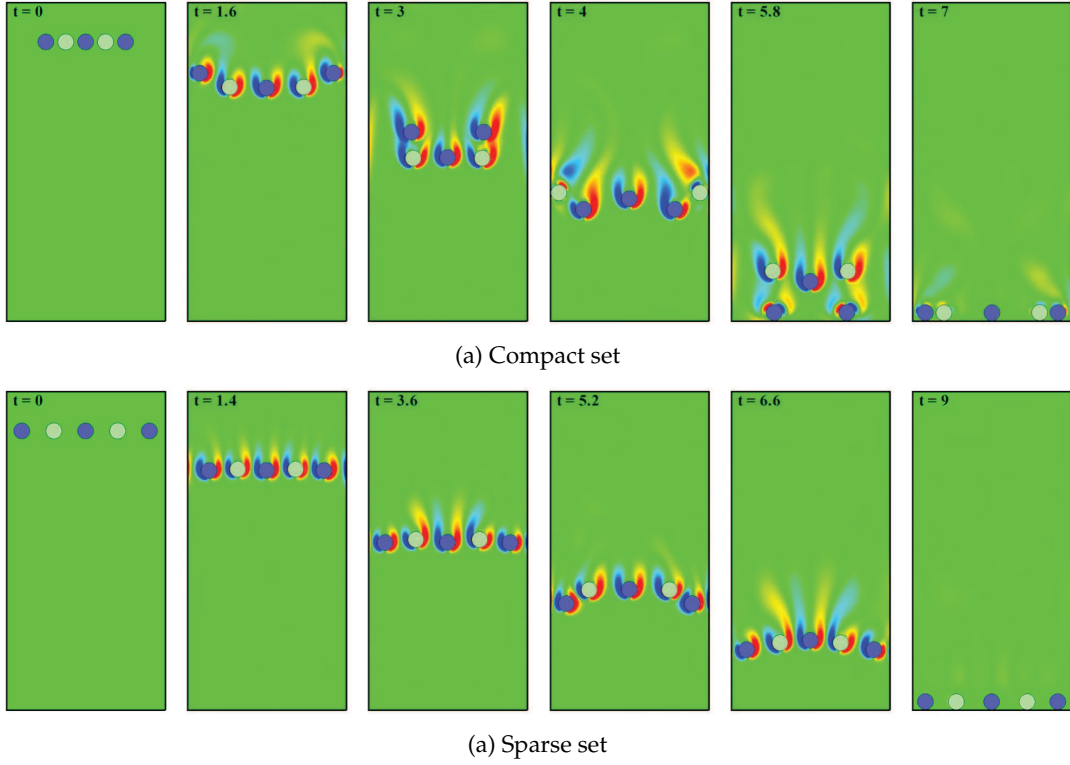


Figure 12: Instantaneous vorticity contours at different instants for sedimentation of five particles.

and they switch their positions twice at the right half part of the tank. For the sparse set, there is no initial particle-particle repulsive force. Therefore, the first and second particles as well as the fourth and fifth particles only fall down with small vibration along the horizontal direction. No position switch occurs during the sedimentation.

Fig. 12 shows several instantaneous vorticity contours at the typical instants. For the compact set, the first particle is close to the left wall at  $t = 1.6$ . It begins to switch its position with the second particle at  $t = 3$ . Then, the second particle is interacting with the left wall at  $t = 4$ . The second position switch occurs at  $t = 5.8$ . When  $t = 7$ , all the particles has reached the tank bottom. For the sparse set, all the particles almost keep in a line before  $t = 1.4$ . After some vibration, they approximately forms an arc at  $t = 6.6$  and reaches the tank bottom at  $t = 9$ .

## 5 Conclusions

In this study, a robust immersed boundary-lattice Boltzmann method for simulation of fluid-structure interaction problems is presented. Compared with the existing IB-LBM, the fractional step technique, which has been employed in the N-S solver, is first intro-

duced into the lattice Boltzmann equation with a forcing term. As a consequence, the non-physical oscillation of body force calculation that is constantly suffered in the traditional IB-LBM can be effectively suppressed. This feature is useful for handling the FSI problems. At the same time, the present IB-LBM can strictly satisfy the no-slip boundary condition by calculating the body force implicitly, which is implemented through the velocity correction method. In addition, the hydrodynamic force on the body can be calculated directly through the relationship between the velocity correction and forcing term.

The current method is first validated by simulating the flows over a fixed circular cylinder and a transversely oscillating circular cylinder. The oscillation of body force calculation is clearly suppressed, and no flow penetration to the body occurs owing to the accurate satisfaction of no-slip boundary condition. Thereafter, the present IB-LBM is employed to deal with various FSI problems, including the vortex-induced vibration of a circular cylinder, an elastic filament flapping in the wake of a fixed cylinder and sedimentation of particles. Based on the numerical results obtained, good agreement between the current results and those in the literature is observed. Therefore, it is indicated that the proposed IB-LBM is robust and effective for simulation of different FSI problems.

## Acknowledgments

J. W. acknowledges the support of the Natural Science Foundation of Jiangsu Province (Grant No. BK20130778) and the National Natural Science Foundation of China (Grant No. 11302104). N. Z. acknowledges the support of the National Program on Key Basic Research Project (Grant No. 2014CB046201). This work is also supported by the Priority Academic Program Development of Jiangsu Higher Education Institutions (PAPD).

## References

- [1] H. H. Hu, Direct simulation of flows of solid-liquid mixtures, *Int. J. Multiphase Flow*, 22:335-352, 1996.
- [2] B. Perot and R. Nallapati, A moving unstructured staggered mesh method for the simulation of incompressible free-surface flows, *J. Comput. Phys.* 184:192-214, 2003.
- [3] T. C. S. Rendall and C. B. Allen, Efficient mesh motion using radial basis functions with data reduction algorithms, *J. Comput. Phys.* 228:6231-6249, 2009.
- [4] C. S. Peskin, Numerical analysis of blood flow in the heart, *J. Comput. Phys.* 25:220-252, 1977.
- [5] H. S. Udaykumar, R. Mittal, P. Rampunggoon and A. Khanna, A sharp interface Cartesian grid method for simulating flows with complex moving boundaries, *J. Comput. Phys.* 174:345-380, 2001.
- [6] D. Kim and H. Choi, Immersed boundary method for flow around an arbitrarily moving body, *J. Comput. Phys.* 212:662-680, 2006.

- [7] R. Mittal, H. Dong, M. Bozkurttas, F. M. Najjar, A. Vargas and A. von Loebbecke, A versatile sharp interface immersed boundary method for incompressible flows with complex boundaries, *J. Comput. Phys.* 227:4825-4852, 2008.
- [8] D. Goldstein, R. Handler and L. Sirovich, Modeling a no-slip flow boundary with an external force field, *J. Comput. Phys.* 105:354-366, 1993.
- [9] M.-C. Lai and C. S. Peskin, An immersed boundary method with formal second-order accuracy and reduced numerical viscosity, *J. Comput. Phys.* 160:705-719, 2000.
- [10] B. E. Griffith, R. D. Hornung, D. M. McQueen and C. S. Peskin, An adaptive, formally second order accurate version of the immersed boundary method, *J. Comput. Phys.* 223:10-49, 2007.
- [11] C. K. Aidun and J. R. Clausen, Lattice-Boltzmann method for complex flows. *Annu. Rev. Fluid Mech.* 42:439-472, 2010.
- [12] Z.-G. Feng and E. E. Michaelides, The immersed boundary-lattice Boltzmann method for solving fluid-particles interaction problems, *J. Comput. Phys.* 195:602-628, 2004.
- [13] Z.-G. Feng and E. E. Michaelides, Proteus: A direct forcing method in the simulations of particulate flows, *J. Comput. Phys.* 202:20-51, 2005.
- [14] X. D. Niu, C. Shu, Y. T. Chew and Y. Peng, A momentum exchanged-based immersed boundary-lattice Boltzmann method for simulating incompressible viscous flows, *Phys. Lett. A*, 354:173-182, 2006.
- [15] J. Zhang, P. C. Johnson and A. S. Popel, An immersed boundary lattice Boltzmann approach to simulate deformable liquid capsules and its application to microscopic blood flows, *Phys. Biol.* 4:285-295, 2007.
- [16] Y. Sui, Y. T. Chew, P. Roy and H. Low, A hybrid method to study flow-induced deformation of three-dimensional capsules, *J. Comput. Phys.* 227:6351-6371, 2008.
- [17] J. Wu and C. Shu, Implicit velocity correction-based immersed boundary-lattice Boltzmann method and its applications, *J. Comput. Phys.* 228:1963-1979, 2009.
- [18] J. Hao and L. Zhu, A lattice Boltzmann based implicit immersed boundary method for fluid-structure interaction, *Comput. Math. Appl.* 59:185-193, 2010.
- [19] F.-B. Tian, H. Luo, L. Zhu, J. C. Liao and X.-Y. Lu, An efficient immersed boundary-lattice Boltzmann method for the hydrodynamic interaction of elastic filaments, *J. Comput. Phys.* 230:7266-7283, 2011.
- [20] K. Suzuki and T. Inamuro, A higher-order immersed boundary-lattice Boltzmann method using a smooth velocity field near boundaries, *Comput. Fluids*, 76:105-115, 2013.
- [21] J. Favier, A. Revell and A. Pinelli, A lattice Boltzmann-immersed boundary method to simulate the fluid interaction with moving and slender flexible objects, *J. Comput. Phys.* 261:145-161, 2014.
- [22] H.-Z. Yuan, X.-D. Niu, S. Shu, M. Li and H. Yamaguchi, A momentum exchanged-based immersed boundary-lattice Boltzmann method for simulating a flexible filament in an incompressible flow, *Comput. Math. Appl.* 67:1039-1056, 2014.
- [23] Y. Hu, H. Yuan, S. Shu, X. Niu and M. Li, An improved momentum exchanged-based immersed boundary-lattice Boltzmann method by using an iterative technique, *Comput. Math. Appl.* 68:140-155, 2014.
- [24] X. Yang, X. Zhang, Z. Li and G. W. He. A smoothing technique for discrete delta functions with application to immersed boundary method in moving boundary simulations. *J. Comput. Phys.* 228:7821-7836, 2009.
- [25] C. Shu, N. Y. Liu and Y. T. Chew, A novel immersed boundary velocity correction-lattice Boltzmann method and its application to simulate flow past a circular cylinder, *J. Comput. Phys.* 226:1607-1622, 2007.

- [26] J. Wu and C. Shu, Simulation of three-dimensional flows over moving objects by an improved immersed boundary-lattice Boltzmann method, *Int. J. Numer. Meth. Fl.* 68:977-1004, 2012.
- [27] J. Wu, C. Shu and N. Zhao, Investigation of flow characteristics around a stationary circular cylinder with an undulatory plate. *Eur. J. Mech. B-Fluid.* 48:27-39, 2014.
- [28] J. Wu, C. Shu and N. Zhao, Numerical investigation of vortex-induced vibration of a circular cylinder with a hinged flat plate, *Phys. Fluids*, 26:063601, 2014.
- [29] S. Xu and Z. J. Wang, An immersed interface method for simulating the interaction of a fluid with moving boundaries, *J. Comput. Phys.* 216:454-493, 2006.
- [30] T. Gao, Y. Tseng and X. Lu, An improved hybrid Cartesian/immersed boundary method for fluid-solid flows, *Int. J. Numer. Meth. Fl.* 55:1189-1211, 2007.
- [31] J. Yang and F. Stern, A simple and efficient direct forcing immersed boundary framework for fluid-structure interactions, *J. Comput. Phys.* 231:5029-5061, 2012.
- [32] L. Schneiders, D. Hartmann, M. Meinke and W. Schröder, An accurate moving boundary formulation in cut-cell methods, *J. Comput. Phys.* 235:786-809, 2013.
- [33] H. T. Ahn and Y. Kallinderis, Strongly coupled flow/structure interactions with a geometrically conservative ALE scheme on general hybrid meshes, *J. Comput. Phys.* 219:671-696, 2006.
- [34] I. Borazjani and F. Sotiropoulos, Vortex-induced vibrations of two cylinders in tandem arrangement in the proximity-wake interference region, *J. Fluid Mech.* 621:321-364, 2009.
- [35] Y. Bao, D. Zhou and J. Tu, Flow interference between a stationary cylinder and an elastically mounted cylinder arranged in proximity, *J. Fluids Struct.* 27:1425-1446, 2011.
- [36] J. C. Liao, D. N. Beal, G. V. Lauder and M. S. Triantafyllou, Fish exploiting vortices decrease muscle activity, *Science*, 302:1566-1569, 2003.
- [37] W.-X. Huang, S. J. Shin and H. J. Sung, Simulation of flexible filaments in a uniform flow by the immersed boundary method, *J. Comput. Phys.* 226:2206-2228, 2007.
- [38] S. K. Kang and Y. A. Hassan, A direct-forcing immersed boundary method for the thermal lattice Boltzmann method, *Comput. Fluids*, 49:36-45, 2011.
- [39] A. Fortes, D. D. Joseph and T. S. Lundgren, Nonlinear mechanics of fluidization of beds of spherical particles, *J. Fluid Mech.* 177:467-483, 1987.